Freight distribution in urban areas: a method to select the most important loading and unloading areas and a survey tool to investigate related demand patterns

Electrochimica Acta 464 (2023) 142862

Contents lists available at ScienceDirect

Electrochimica Acta

journal homepage: www.journals.elsevier.com/electrochimica-acta

Engineering copper nanoparticle electrodes for tunable electrochemical reduction of carbon dioxide

Juqin Zeng [a,b,*], Manlio Mignosa [a,b], Nicolò B.D. Monti [a,b], Adriano Sacco [a,**], Candido F. Pirri [a,b]

[a] Center for Sustainable Future Technologies @POLITO, Istituto Italiano di Tecnologia, Via Livorno 60, 10144 Turin, Italy
[b] Department of Applied Science and Technology, Politecnico di Torino, C.so Duca degli Abruzzi 24, 10129 Turin, Italy

ARTICLE INFO

Keywords:
Carbon dioxide utilization
Electrocatalysis
Copper nanoparticle
Ethylene
Catalyst loading

ABSTRACT

The electrochemical conversion of CO_2 catalyzed by copper (Cu)-based materials is widely reported to produce different valuable molecules, and the selectivity for a specific product can be achieved by tuning the characteristics of catalytic materials. Differing from these studies on materials, the present work focuses on the engineering of gas diffusion electrodes in order to properly modify the selectivity, particularly by changing the Cu nanoparticle catalyst loading of the electrodes. Low catalyst loadings ($\leq$ 0.25 mg cm^{-2}) favor CH_4 production, and intermediate ($\sim$ 1.0 mg cm^{-2}) loadings shift the selectivity toward C_2H_4. Eventually, larger values ($\geq$ 2.0 mg cm^{-2}) promote CO production. Detailed analyses reveal that both bulk and local CO generation rates, and charge transfer mechanism are responsible for the observed loading-dependent selectivity. The present work provides a new strategy for steering the CO_2RR selectivity by simple electrode engineering beyond material development.

1. Introduction

The reduction of CO_2 into useful fuels and chemicals through electrochemical means is both economically and environmentally appealing. This innovative technology has the potential to establish a sustainable carbon cycle and combat climate changes, while also storing renewable energy [1,2]. Despite over a decade of global efforts by chemists, physicists, and engineers, commercializing this process is difficult due to the complex mechanism of CO_2 reduction reaction (CO_2RR), which results in a variety of products like carbon monoxide (CO), formic acid (HCOOH), methane (CH_4), ethylene (C_2H_4), ethanol (C_2H_5OH) and methanol (CH_3OH) [3–9]. Among them, CO and HCOOH can be obtained with very high selectivity ($>$ 90%), and the use of gas diffusion electrodes is consider a key factor to go beyond the state-of-the-art performance and the stability issue is the main challenge for commercialization [10]. Instead, state-of-the-art methods for electrochemical CO_2 conversion to some products such as CH_4, C_2H_4 and C_2H_5OH still call for electrocatalysts to enhance the selectivity by improving the CO intermediate production and blocking hydrogen formation [10,11].

Nonetheless, these products are significant for various industries. For instance, CH_4, which makes up the largest part of natural gas, provides 24% of the world's energy and has a well-established system for storage, transportation, and consumption [12,13]. C_2H_4, on the other hand, is widely used in the production of materials such as ethylene glycol, ethylene oxide, and polyethylene, which is produced mainly through the steam cracking of naphtha and natural-gas-derived ethane in the current industries. However, this process requires a lot of energy and results in a considerable amount of CO_2 emissions [14]. The production of these molecules through electrochemical reduction of CO_2 has high economic and environmental significance, but still poses challenges in terms of catalytic materials and processes. Copper (Cu) has been found to be a unique catalyst among the studied metals, capable of directing the selectivity of CO_2RR towards C_1 and C_2 chemicals. Studies suggest that the selectivity of Cu catalysts for C_1 and C_2 products, particularly hydrocarbons, can be controlled through various methods, such as surface engineering, coordination control, modification of the catalyst/electrolyte interface, and process design. This includes techniques such as manipulating particle size [15], surface roughness [16,17], facet [18], oxidation state [19–22], grain boundary [23], Cu coordination number [24], local pH [25], controlling CO_2 availability [12] and using tandem catalysis [26,27]. The size of Cu nanoparticles shows dramatic effects on the catalytic activity and selectivity of the catalysts during CO_2 electroreduction, with remarkable enhancement in the production of H_2 and

* Corresponding author at: Department of Applied Science and Technology, Politecnico di Torino, C.so Duca degli Abruzzi 24, 10129 Turin, Italy.
** Corresponding author at: Center for Sustainable Future Technologies @POLITO, Istituto Italiano di Tecnologia, Via Livorno 60, 10144 Turin, Italy.
E-mail addresses: juqin.zeng@polito.it (J. Zeng), adriano.sacco@iit.it (A. Sacco).

https://doi.org/10.1016/j.electacta.2023.142862
Received 19 June 2023; Received in revised form 8 July 2023; Accepted 9 July 2023
Available online 10 July 2023

CO with decreasing Cu particle size [15]. Studies have shown that the roughness of a surface has a significant impact on the selectivity of CO_2 reduction towards C_{2+} products. This is because roughness causes the confinement of gaseous intermediates like CO within mesopores, which is key in determining the selectivity. Theoretical and experimental studies have found that the Cu (111) facet affects the pathways for generating CH_4 during CO_2 reduction, while the Cu (100) facet directs the C—C coupling step for the production of C_{2+} products. Additionally, the composition of the Cu catalyst surface plays a crucial role in determining the selectivity and activity towards C_2H_4 or CH_4 [28]. The exact nature of the active site of the catalyst, specifically the ratio of Cu oxidation species ($Cu^{\delta+}$) to metallic species (Cu^0), is still a matter of debate. Nevertheless, several studies have shown that the ratio of $Cu^{\delta+}$ to Cu^0 can significantly influence the selectivity between CH_4 and C_2H_4 under the same conditions. Cu^0 sites tend to favor the hydrogenation of CO into CH_4, while Cu^0/Cu^+ hybrid sites tend to promote the dimerization of CO into C_2H_4. Different coordination numbers of Cu were found to have different hydrocarbon selectivity, with low coordination numbers promoting the production of CH_4.

In this study, instead of focusing on material properties, we demonstrate that it is possible to tune the selectivity of CO_2RR towards C_1 and C_2 products by simply modifying the catalyst loading on the electrodes. This strategy was partially studied on copper-based catalysts such as copper phosphate [29] and copper(II) phthalocyanine/carbon catalysts [24]. In the former work, the copper phosphate is reduced to metallic Cu nanoparticles at low loading condition, favoring *CO hydrogenation to CH_4 production, while metallic Cu nanoparticles decorated with $Cu_3(PO_4)_2$ are produced at high $Cu_3(PO_4)_2$ loading condition, promoting the dimerization of *CO to C_2H_4 formation. Hence, the effect of catalyst loading is actually considered to be the effect of the surface composition of derived catalysts in this literature work. In the latter work, carbon particles are used to isolate and prevent the agglomeration of low coordination number Cu clusters formed during the in-situ reduction of a copper(II) phthalocyanine, enhancing the *CO hydrogenation and boosting the selectivity toward CH_4. Strictly speaking, this literature work can be considered to have a focus on a composite catalyst of Cu clusters and carbon nanoparticles with various Cu/C ratios. On the contrary, in the present study, commercial Cu nanoparticles (NPs) are the only composition of the catalyst layer beyond a 17 wt.% of Nafion, and only the Cu NPs loading varies for different electrodes. The Cu NPs gas diffusion electrodes (GDE) were then tested in a flow reactor with highly alkaline electrolyte and a gaseous CO_2 feed. This setup ensures a high rate of CO_2 diffusion and shortens the distance between the CO_2 gas and the catalyst layer, allowing to obtain industrially-relevant current densities larger than 1 A cm^{-2} at cell voltages lower than 4.0 V. The electrodes demonstrated a controlled selectivity towards CH_4, C_2H_4, and CO, which was likely due to the combination of the bulk and local CO generation rates on the electrode and at the active sites, respectively.

2. Experimental

2.1. Materials

The following materials were obtained from Merck: Copper nanoparticles of 25 nm size (CAS Number: 7440–50–8), copper nanoparticles with a size range of 40–60 nm (CAS Number: 7440–50–8), a 5 wt% solution of Nafion® 117 (CAS Number: 31,175–20–9), isopropanol (CAS Number: 67–63–0), and potassium hydroxide with a purity of 84 wt% or greater (CAS Number: 1310–58–3). They were used as received, unless otherwise indicated.

2.2. Preparation of the electrodes

The method used to create the electrodes is extremely crucial and has a significant impact on their electrochemical performance [30,31]. In this study, a straightforward drop-casting approach was employed to place Cu NPs on a carbon gas diffusion layer (GDL) substrate, which allows for precise control over the catalyst quantity. Electrodes with varying Cu loadings of 0.25, 0.5, 1.0, 2.0, and 3.0 mg cm^{-2} were created, all with a consistent 17 wt.% Nafion content in the dry electrode. Two different sized Cu NPs, 25 nm and 50 nm, were examined. The electrodes featuring 25 nm NPs are labeled as Cu25_x and those with 50 nm NPs are referred to as Cu50_x, where x represents the respective catalyst loading of 0.25, 0.5, 1.0, 2.0, or 3.0. A standard preparation involves thoroughly mixing a specific quantity of Cu NPs, Nafion solution, and 150 μL of isopropanol through sonication. The resulting homogeneous mixture was then applied to a GDL (SIGRACET 28BC, SGL Technologies) and left to dry at room temperature for an entire night to eliminate the solvents.

2.3. Physical and chemical characterizations of Cu NPs and prepared electrodes

Morphological characteristics of the samples were obtained through Field emission scanning electron microscopy (FESEM Supra 40, Zeiss, Oberkochen, Germany) equipped with Oxford EDS microanalysis (Liquid-N_2 cooled Si(Li) detector). X-ray diffraction (XRD) patterns of the samples were acquired with a PANalytical X'Pert Pro-diffractometer (Cu-Kα radiation, 40 kV and 30 mA) equipped with an X'Celerator detector.

2.4. Electrochemical tests and product analysis

The electrochemical performance of the electrodes was initially evaluated through cyclic voltammetry (CV) and electrochemical impedance spectroscopy (EIS) measurements. These tests were conducted in a flow cell configuration (Scheme S1a), using a CHI760D potentiostat at room temperature. A Pt wire served as the counter electrode, while a Ag/AgCl (3 M Cl^-) electrode acted as the reference. The working electrode was the Cu NP-coated GDL electrode with an active area of 0.25 cm^2. A 1.0 M KOH aqueous solution that was purged with argon (Ar) was used as the electrolyte. CV measurements were carried out over a potential range from 0.6 V to −0.6 V relative to the reversible hydrogen electrode (RHE) at a scan rate of 100 mV s^{-1}. After that, all potentials mentioned in this work are expressed in terms of RHE and adjusted according to the Nernst equation: E (V vs. RHE) = E (V vs. Ag/AgCl) + $E^{\circ}_{Ag/AgCl}$ + 0.059 * pH, where $E^{\circ}_{Ag/AgCl}$ is the standard potential of the reference electrode, E (V vs. Ag/AgCl) is the applied potential against the reference electrode, pH is the pH value of the electrolyte, and E (V vs. RHE) is the reported potential. Furthermore, CV tests were also conducted over a narrow potential range of 0.036 V to 0.236 V at scan rates of 5, 10, 20, 30, 40, 50, 60, 80, and 100 mV s^{-1} to estimate the double layer capacitance (C_{dl}) of the electrode. The EIS measurements were performed over a frequency range of $10^{-1} - 10^5$ Hz with an AC signal of 10 mV of amplitude at −0.4 V in 1.0 M KOH electrolyte, in order to gain insight into the electrical properties of the electrodes and the electrode/electrolyte interface.

The CO_2 electrolysis was performed using a chronopotentiometry (CP) method with a CHI760D potentiostat. The performance of all electrodes was evaluated based on the electivity of CO_2RR in a 1.0 M KOH electrolyte using a flow cell configuration, as shown in Scheme S1a and discussed in detail in our previous work [32]. Additionally, the Cu25_1.0 electrodes were further tested in a two-electrode setup (Scheme S1b) at various current densities in a 1.0 M KOH electrolyte, using a commercially available iridium-coated titanium plate (Ir-MMO) as the anode and an as-prepared Cu electrode as the cathode. The quantification of gaseous products was done using a micro gas chromatograph (μGC) equipped with two Rt-Molsieve 5A and Rt-Q-Bond columns, and a micro thermal conductivity detector (TCD) for each module. A high-performance liquid chromatograph (HPLC) was also used to analyze the liquid products. The HPLC was equipped with a ReproGel column and an ultraviolet-visible (UV–Vis) detector that was set at 210 nm, with a mobile phase of 9.0 mM H_2SO_4 and a flow rate of

1.0 mL min^{-1}. The faradaic efficiency (FE) was calculated using Eq. (1), which involves dividing the amount of charge required to produce a specific number of moles (N) of a product by the total charge consumed during the corresponding reduction period (Q)

$$FE = \frac{nNF}{Q} \times 100\% \quad (1)$$

where n is the mole of electrons required to obtain one mole of this product ($n = 2$ for CO, $HCOO^-$ and H_2; $n = 12$ for C_2H_4 and C_2H_5OH; $n = 8$ for CH_4 and CH_3COO^-), and F is the Faraday constant that is 96,485 C mol^{-1}.

The energy efficiency (EE) for a specific product was calculated using Eq. (2),

$$EE = \frac{E^{\circ}_{anode} - E^{\circ}_{cathode}}{cell\ voltage} \times FE \quad (2)$$

where FE is the faradaic efficiency of this product in percentage, E°_{anode} is the equilibrium potential (V vs. RHE) of water oxidation, $E^{\circ}_{cathode}$ is the equilibrium potential (V vs. RHE) of CO_2 reduction to a specific product [33].

3. Results and discussion

3.1. Study of physical and chemical properties of Cu NPs and electrodes

FESEM has been performed on the commercial Cu nanoparticles in order to confirm the morphology of the samples. As shown in Fig. 1, the particles have expected average sizes, 25 nm and 50 nm, respectively, as indicated in datasheet of the commodities. The nanoparticles agglomerate, and form secondary particles that are much bigger.

The morphology of the 25 nm and 50 nm electrodes has also been studied, as shown in Figures S1 and S2, respectively. The Cu NPs agglomerations are more visible at higher loadings, and they are distinguishable from carbon black nanoparticles of the microporous layer of GDL (Figure S3). At the lowest loading of 0.25 mg cm^{-2}, many carbon black particles with a uniform size are observed, as can be seen from EDX mapping on Cu25_0.25 in Figure S4. With increasing the loading, the Cu agglomerations dominate the electrode surface at loadings $\geq$1.0 mg cm^{-2}, which can be observed by EDX mapping on Cu25_1.0 in Figure S5. XRD analysis has been conducted on the as-prepared electrodes with 3.0 mg cm^{-2}. The electrodes with the highest loading were used for XRD measurements in order to obtain better signal of the catalyst layer. As displayed in Figure S6, both Cu25 and Cu50 electrodes show intensive diffraction peaks associated with metallic Cu, and only a small fraction of cuprous oxide (Cu_2O) is also observed due to the oxidation of Cu in air.

3.2. Study of electrochemical properties of Cu electrodes

Before conducting any experiments, the prepared electrodes underwent a stabilization process in which they were subjected to 30 cycles from 0 V to −0.6 V relative to the reversible hydrogen electrode (RHE) with a scan rate of 100 mV s^{-1}. As shown in Figure S7, at the end of the process, the CV curves become stable, meaning that the surface oxide is mainly reduced to metallic Cu. The metallic Cu is the main active phase under the CO_2RR potentials, which are more negative than −0.6 V. Concisely, this process aims to reduce the little oxide on the surface in order to obtained the double layer capacitance of the Cu electrodes with metallic surface, which should be the real surface under the CO_2RR conditions. After stabilization, cyclic voltammetry tests were conducted at various scan rates of 5–100 mV s^{-1} in a potential range where no electrochemical reactions take place, to calculate the double-layer

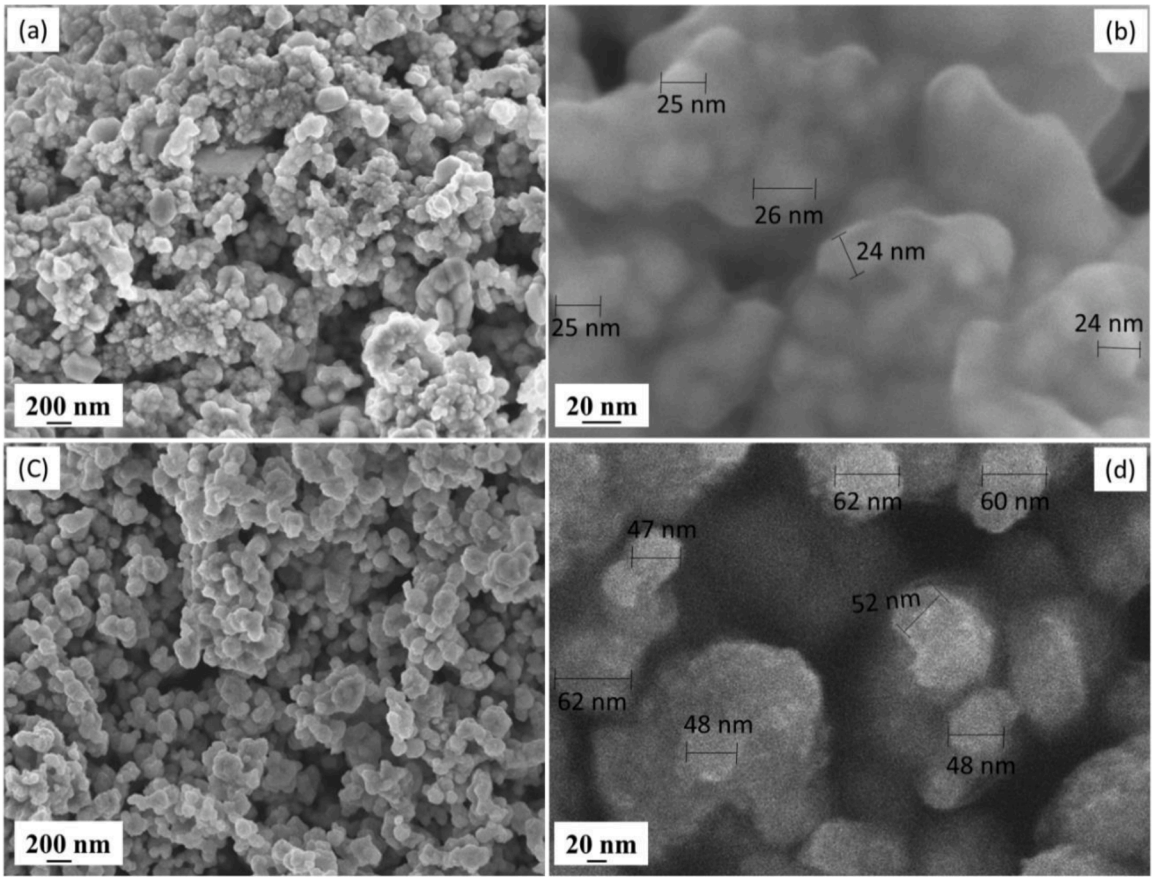

Fig. 1. FESEM images of Cu25 (a and b) and Cu50 (c and d) nanoparticles.

capacitance (C_{dl}) of the electrode. [34,35]. The C_{dl} is estimated by plotting the geometric current densities against scan rates and finding the slope of the linear fit. The calculated C_{dl} values for the Cu25_0.25, Cu25_0.5, Cu25_1.0, Cu25_2.0, and Cu25_3.0 electrodes were found to be 1.4, 2.1, 2.7, 7.4, and 7.8 mF cm^{-2} respectively, as shown in Fig. 2 for the Cu25_1.0 electrode. According to the literature [36], an ideally flat Cu foil has a C_{dl} value of 28 μF cm^{-2}, and the electrochemical active surface area (ECSA) of the electrodes can be obtained via dividing the C_{dl} values by 28 μF cm^{-2}. This method is widely used to evaluate the ECSA of Cu electrodes [34,37], despite the obtained ECSA values are not totally precise, since the C_{dl} of the ideally flat Cu slightly varies in different electrolytes [38]. However, this method is valid to compare different electrodes in the same work. The calculated ECSA are 50, 75, 96, 264 and 278 cm^2 for each geometry unit (cm^2) of Cu25_0.25, Cu25_0.5, Cu25_1.0, Cu25_2.0 and Cu25_3.0 electrodes, respectively. Similarly, the evaluated C_{dl} values are 1.2, 2.0, 3.0, 3.5 and 8.6 mF cm^{-2} for Cu50_0.25, Cu50_0.5, Cu50_1.0, Cu50_2.0 and Cu50_3.0 electrodes, respectively, corresponding to ECSA of 43, 71, 107, 125 and 307 cm^2 for each geometric cm^2. In general, the ECSA of the Cu25 electrode is slightly higher than that of the Cu50 one at the same loading, and the ECSA increases with increasing the Cu loading for both Cu25 and Cu50 samples. This is due to the fact that smaller particles potentially have a higher surface-to-mass ratio compared to larger ones, and a higher loading has more particles available for building the electrolyte/catalyst interface.

The electrochemical behaviors of the Cu electrodes were analyzed by conducting CV experiments in a 1.0 M KOH electrolyte that was purged with Ar. Fig. 3a and 3b present the voltammograms of the Cu25 and Cu50 electrodes, respectively. In the potential range between 0.25 and 0.6 V, peaks related to the redox reactions of Cu species are observed [39]. The cathodic scan reduces Cu oxide species to metallic Cu, while the anodic scan re-oxidizes Cu to Cu oxides. The intensity of the redox peaks increases as the loading of Cu NPs increases, as expected. Within the potential range of −0.2 to −0.6 V, only hydrogen evolution reaction (HER) is observed due to the Ar purging of the electrolyte during measurement. In general, as the amount of catalyst increases, the geometric current density also rises. By dividing the current by the electrochemical active surface area (ECSA), the specific current density, which reflects the catalytic activity of the Cu NPs on the electrode, can be obtained. As depicted in Fig. 3c, the activity of the Cu25 NPs increases with a rise in loading until it reaches 0.5 mg cm^{-2}, but the trend then reverses when the loading exceeds 1.0 mg cm^{-2}. In general, Cu50 NPs exhibit lower activity compared to Cu25 NPs at similar loading levels (as seen in Fig. 3d). Additionally, the impact of mass loading on the activity of Cu50 NPs is much less significant than its impact on Cu25 NPs.

EIS was also conducted to analyze the electrochemical characteristics of the Cu electrodes in an Ar-purged 1.0 M KOH electrolyte. Fig. 4a and 4b display the Nyquist plots of the impedance of Cu25 and Cu50 electrodes, respectively. The impedance spectra of all samples are dominated by the charge transfer process, which has a much greater resistance than the high-frequency charge transport process [40]. Moreover, for both sets of electrodes, as the loading increased, the impedance values decreases, which aligns with the trend observed in the CV measurements (Fig. 3a and 3b) where the larger the current, the lower the impedance. By using the equivalent circuit shown in the inset of Fig. 4 [5], the charge transfer resistance (R_{ct}) values were obtained and displayed in Fig. 4c and 4d for Cu25 and Cu50 electrodes, respectively. As expected, the Rct values decrease with increasing NPs loading. However, when the charge transfer time constant (τ) values were calculated by multiplying the R_{ct} values by the corresponding C_{dl} values [3], it is observed (as shown in Fig. 4c and 4d) that the trend of τ exhibits a minimum. This indicates that the charge transfer mechanism is dominated by capacitive effects [41], which slow down the reduction process at high loadings. The minimum τ value is found to be at a loading of 0.5–1.0 mg cm^{-2} for Cu25 electrodes, implying that these electrodes have faster faradaic processes. For Cu50 electrodes, the τ value increases with increasing catalyst loading, except for the lowest loading of 0.25 mg cm^{-2}.

3.3. CO_2RR tests and product distribution on various Cu electrodes

The activity of the Cu electrodes was compared through CO_2 electrolysis performed at constant cathodic current densities of 200 and 267 mA cm^{-2} in 1.0 M KOH electrolyte. Figures S8a and S8c depict the typical time-potential curves at current densities of 200 mA cm^{-2} and 267 mA cm^{-2} for the Cu25_0.5 electrodes, respectively. All other electrodes exhibit similar curves, with potentials that are comparably negative as the current density increases. Figures S8b and S8d present the distribution of gas products as a function of time at current densities of 200 and 267 mA cm^{-2}, respectively. CO, CH_4 and C_2H_4 are observed to be the main products of CO_2RR, while HER is found to dominate and increase over time.

The selectivity of different Cu25 electrodes in 1.0 M KOH at current densities of 200 and 267 mA cm^{-2}, taking into account both gas and liquid products, is presented in Figs. 5a and 5b, respectively, and the detailed data are listed in Table S1. At both current densities, the selectivity for C_2H_4 rises as the catalyst loading increases from 0.25 to 1.0 mg cm^{-2} and then decreases as the loading increases further, which is in contrast to the trend of H_2 production. The selectivity of CO increases with increasing Cu loading, becoming the dominant product at

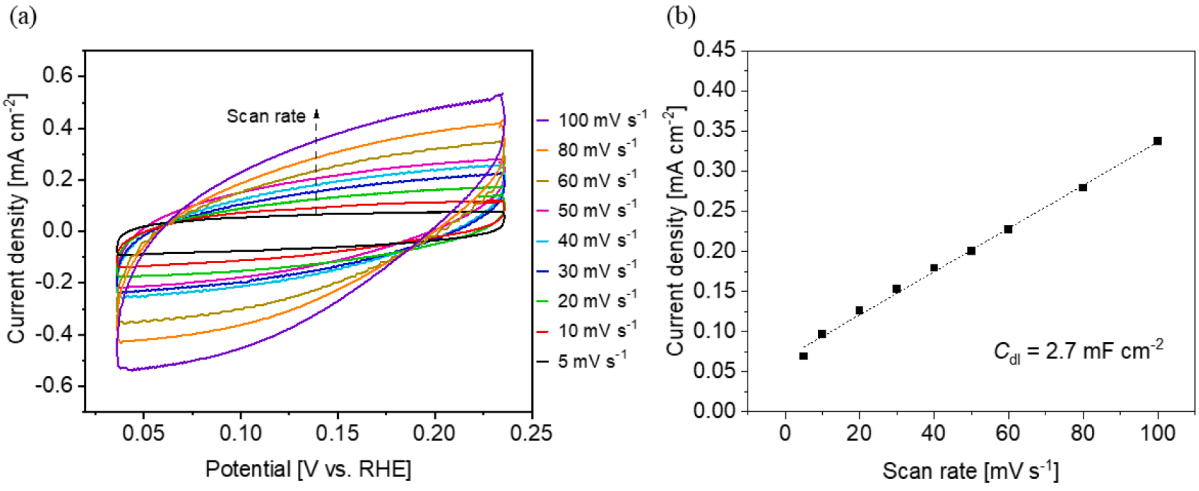

Fig. 2. Determination of C_{dl} in Ar-purged 1.0 M KOH: (a) representing voltammograms on Cu25_1.0 electrode; (b) current density as function of scan rate.

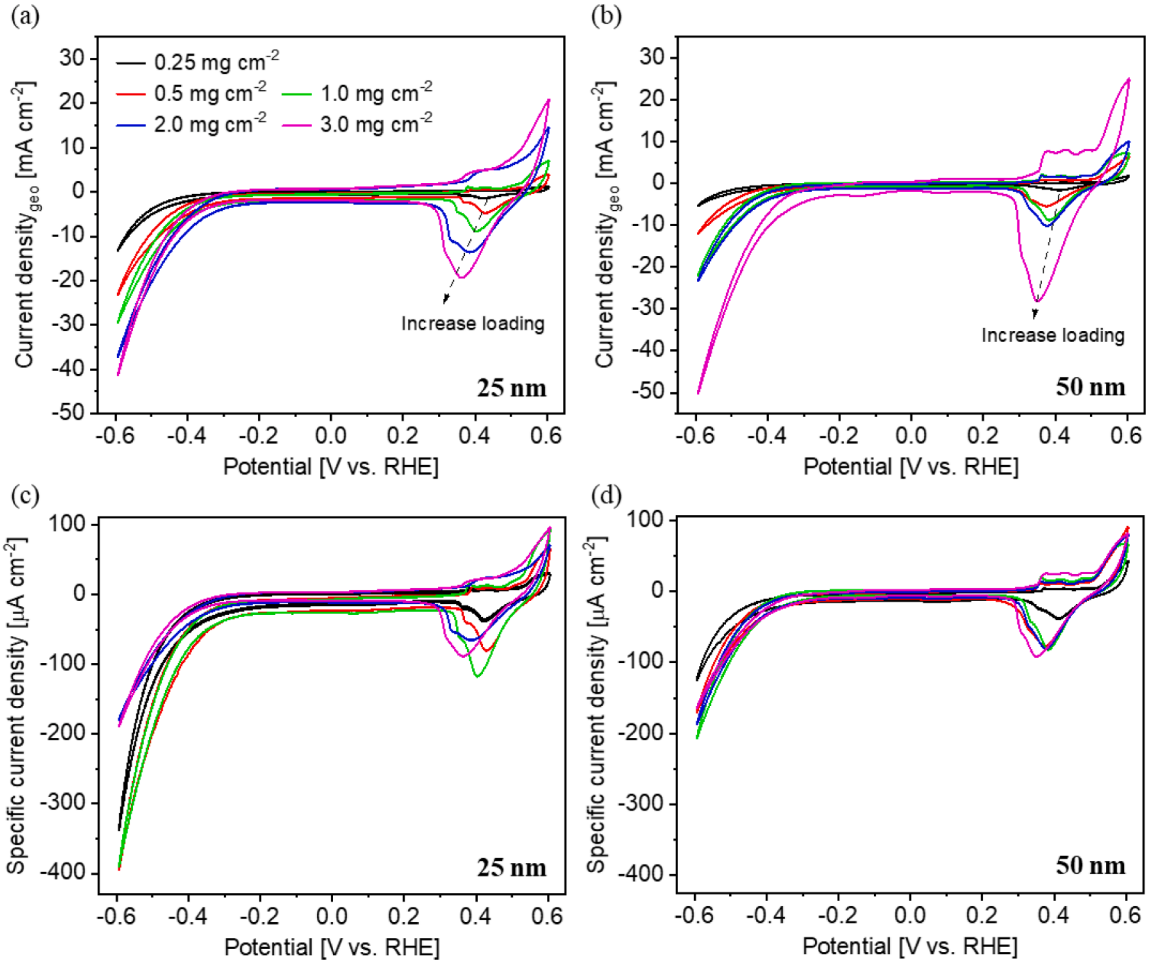

Fig. 3. Voltammograms in Ar-purged 1.0 M KOH: geometric current density on (a) Cu25 and (b) Cu50 electrodes; ECSA-normalized current density on (c) Cu25 and (d) Cu50 electrodes.

higher loadings ($\geq$ 2.0 mg cm^{-2}). On the other hand, CH_4 is prominently formed at the lowest loading and quickly decreases with increasing Cu loading. To comprehend the changes in selectivity, the equivalent geometric (bulk) CO generation and dimerization rates are calculated and normalized (local) by the ECSA at various current densities. The equivalent bulk CO generation and dimerization rates on all Cu25 electrodes at 200 and 267 mA cm^{-2} are presented in Fig. 5c and 5d, respectively. At both current densities, a notable increase in the CO generation rate can be observed as the Cu loading increases from 0.25 to 1.0 mg cm^{-2}, followed by a quasi-plateau. The CO dimerization rate is also observed to increase with the increase in the CO generation rate at relatively low loadings ($\leq$ 1.0 mg cm^{-2}), which is reasonable given that a higher CO concentration promotes CO dimerization [42,43]. At higher loadings, the CO dimerization rate decreases, even though the CO generation rate does not show any decrease. Most of the formed CO tends to release rather than undergo further dimerization. To shed light on the local CO concentration on the active sites, the CO generation and dimerization rates were normalized by the ECSA value for each Cu25 electrode, as shown in Fig. 5e and 5f for current densities of 200 and 267 mA cm^{-2}, respectively. The local CO generation rate at the active sites is relatively lower at high loadings ($>$ 1.0 mg cm^{-2}), which may explain the decrease in the CO dimerization rate and the increase in CO release. It is noteworthy that the highest CH_4 selectivity is observed at the lowest catalyst loading, which could be due to the high dispersion of Cu NPs on the carbon black layer of the GDL. This results in more distanced active sites, suppressing CO dimerization and promoting its hydrogenation, representing a new approach for improving CH_4 selectivity and differing from the methods described in previous studies. According to a study by Xu et al. [24], a low coordination Cu catalyst, which was created by distributing Cu clusters on a GDL, resulted in CH_4 formation even with high pH electrolytes. Bai et al. [19] synthesized two copper catalysts with well-controlled and distinct surface structures that showed unique adsorption configurations of CO intermediates. On low coordination Cu^0 sites, bridge-adsorbed CO intermediates are more likely to be hydrogenated and reduced to CH_4, while on local Cu^0/Cu^+ sites, bridge-adsorbed and linear-adsorbed CO molecules coexist and tend to form C_2H_4. Zhang et al. [21] showed that the selectivity between CH_4 and C_2H_4 can be controlled by adjusting the composition of Cu surface species on gas-diffusion electrodes. A higher $Cu^{\delta+}/Cu^0$ ratio leads to better selectivity for CH_4 (65.4%) through the hydrogenation of *CO, while a low $Cu^{\delta+}/Cu^0$ ratio results in higher selectivity for C_2H_4 (80.1%) through C–C coupling. The selectivity for C_2H_4 increases and the selectivity for CH_4 decreases as the proportion of Cu oxide species decreases. Zhou et al. [44] stabilized cationic Cu ions in a CeO_2 matrix, which significantly increased the selectivity for CH_4 by improving the adsorption stability of *CO intermediates. In this study, the observed loading-dependent selectivity provides an easy way to prepare electrodes for producing specific products. To maximize CH_4 formation, a more advanced method such as ultrasonic spray coating should be used to create homogeneous electrodes with very low Cu NP loading.

The Cu50 electrodes display a higher selectivity for C_2H_4 compared to Cu25 electrodes when the catalyst loading is less than 1.0 mg cm^{-2} (Fig. 6a and 6b, Table S2), with a much lower selectivity for CH_4 at 0.25 mg cm^{-2}. Higher CH_4 selectivity was obtained at lower loadings than

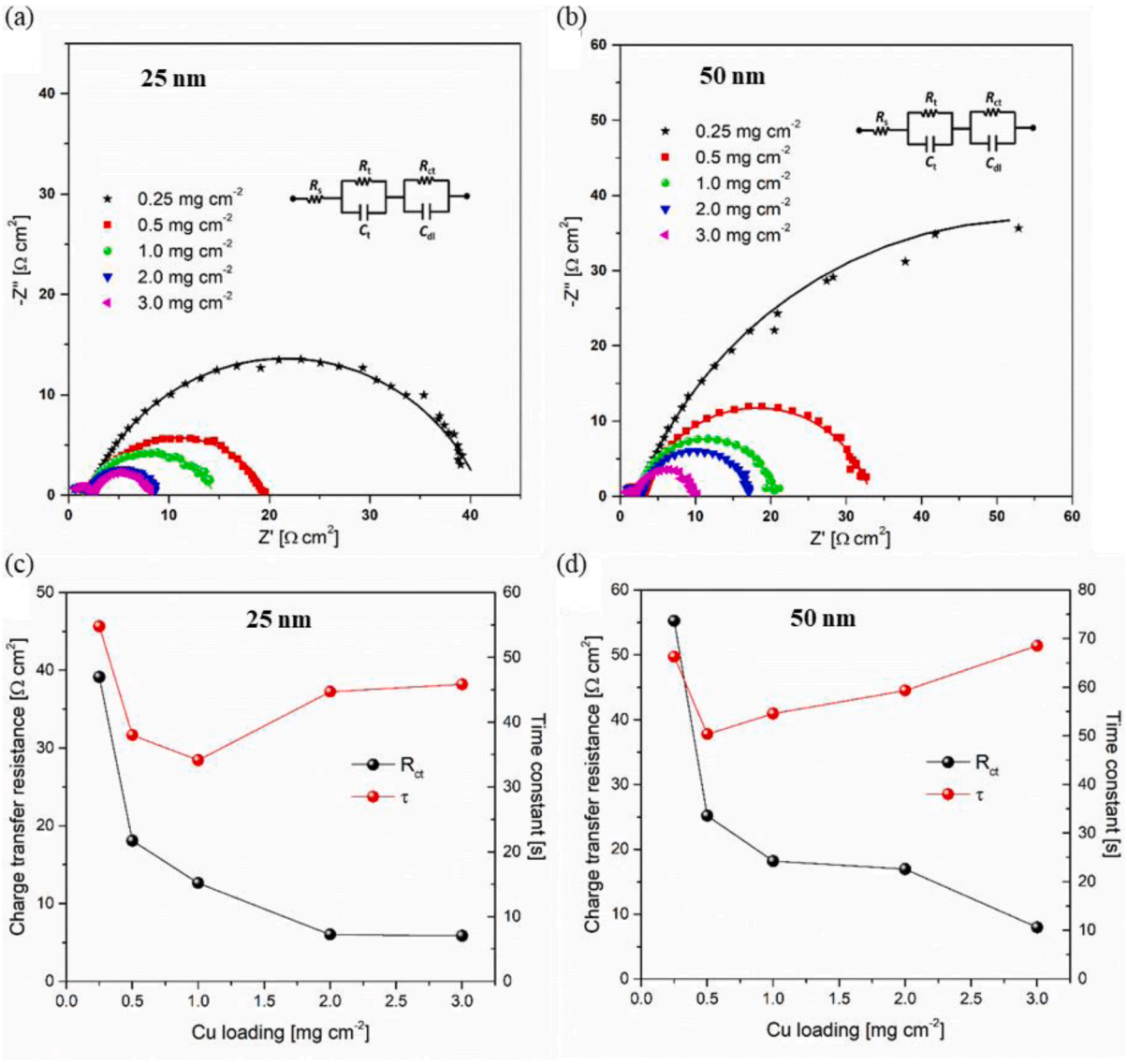

Fig. 4. EIS measurements in Ar-purged 1.0 M KOH: Nyquist plot of (a) Cu25 and (b) Cu50 electrodes (the points represent experimental data, the lines are the curves obtained through the fitting procedure using the equivalent circuit shown as inset); charge transfer resistance R_{ct} (left axis) and time constant τ (right axis) obtained through the fitting procedure for (c) Cu25 and (d) Cu50 electrodes.

0.25 mg cm^{-2} (data not shown). Low FE values are maintained for all loadings in the HER process, and the CO selectivity consistently increases as the catalyst loading increases at both current densities. With respect to the Cu25 NPs electrodes, the trend of selectivity change with loading remains the same for the Cu50 NPs ones, despite the significant differences in their behaviors. Fig. 6c and 6d depict the equivalent CO generation and dimerization rates on different Cu50 electrodes at 200 and 267 mA cm^{-2}, respectively. At both current densities, the CO generation rate steadily increases as the Cu loading increases from 0.25 to 3.0 mg cm^{-2}, while the CO dimerization rate shows an opposite trend. The CO generation and dimerization rates are normalized by the ECSA value of each Cu50 electrode in Fig. 6e and 6f at 200 and 267 mA cm^{-2} to understand the CO concentration at the active sites. It is observed that the local CO generation at the active sites decreases at high loadings, leading to a corresponding decrease in the CO dimerization rate.

Additionally, it's worth mentioning that, for Cu25 electrodes, the trend of the local CO dimerization rate is in line with the charge transfer time constant that was discussed earlier in Fig. 3. In other words, the larger the local dimerization rate, the shorter the time constant. This holds true for Cu50 electrodes as well, except for the smallest loading of 0.25 mg cm^{-2}. This correlation supports the idea that the slower flow of charges from the electrode decelerates the further reduction of CO near the catalytic sites, hindering the formation of C_2 products. A comprehensive examination was carried out on the Cu25_1.0 electrodes in a two-electrode configuration across a range of current densities from 150 to 1200 mA cm^{-2}. Fig. 7a displays the product distribution at all current densities, and Table S3 lists the detailed data. The CO selectivity decreases as the current density increases, while CH_3CH_2OH production generally increases with an increase in current density and reaches 19% at 1200 mA cm^{-2}. FE_{C2H4} attains desirable values (> 35%) at current densities above 300 mA cm^{-2}, with a peak of 46% when a current density of 600 mA cm^{-2} is used. At all the studied current densities, the selectivity for CH_3COO^-, $HCOO^-$, and CH_4 remains low (< 5%), and FE_{H2} remains below 20%. It's worth noting that the selectivity for C_2 products improves with increasing current density (Fig. 7b), resulting in an increase in the C_2/C_1 product ratio.

The selectivity for C_2 products is nearly 60% at high current densities of 800–1200 mA cm^{-2}, at relatively low cell voltages less than 4.0 V, as shown in Fig. 7d. As seen in Fig. 7c, there is a significant correlation between the current density and the CO generation rate, as well as the

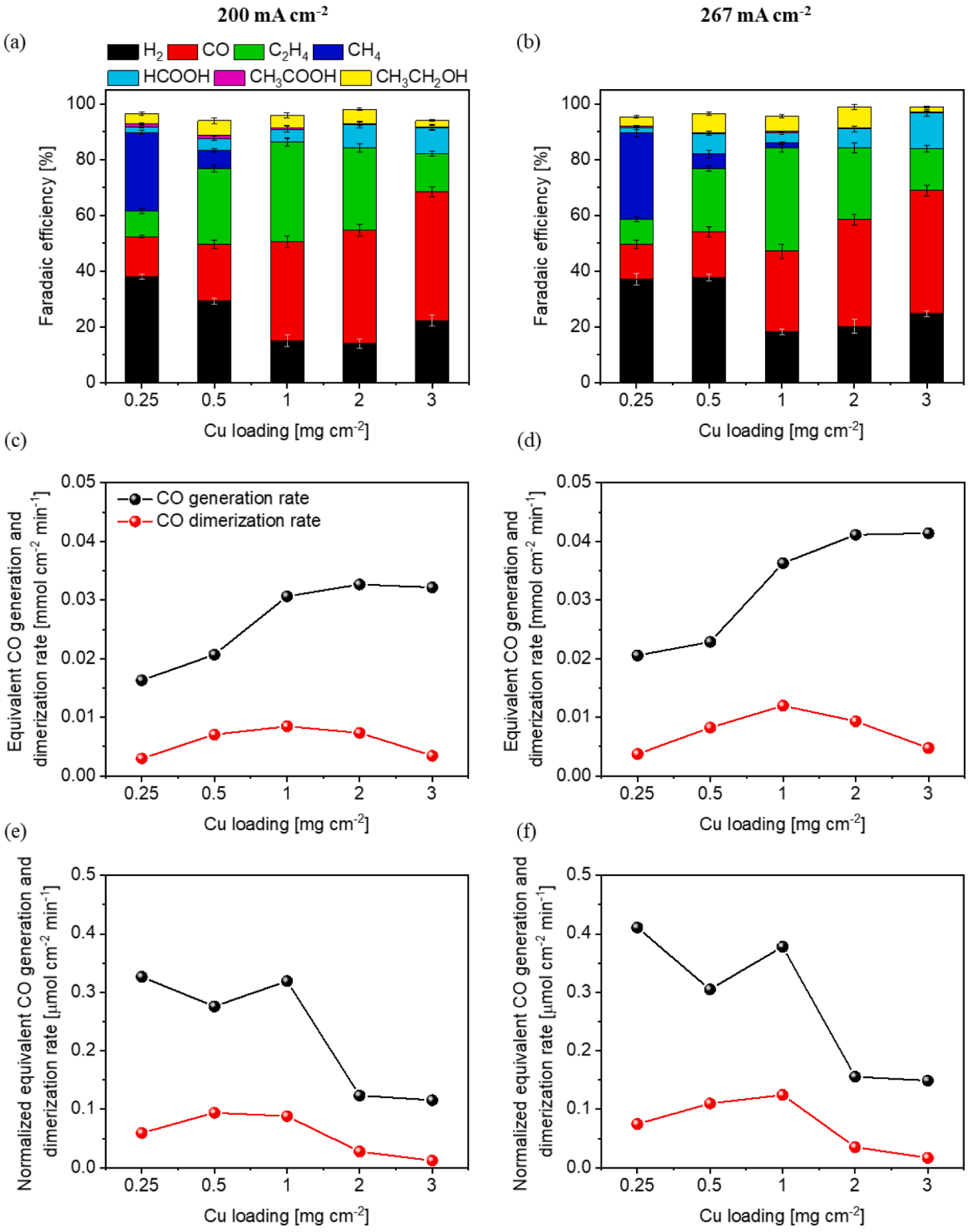

Fig. 5. Comparison of 25 nm NPs electrodes with different loadings: at 200 mA cm^{-2} (a) selectivity, (c) equivalent bulk CO generation and dimerization rates and (e) ECSA-normalized equivalent CO generation and dimerization rates; at 267 mA cm^{-2} (b) selectivity, (d) equivalent bulk CO generation and dimerization rates and (f) ECSA-normalized equivalent CO generation and dimerization rates. Each electrode was tested at least twice. The bulk and ECSA-normalized equivalent CO generation and dimerization rates in (c)-(f) were calculated based on the average values of selectivity of at least two sets of experiments at each catalyst loading and current density.

CO dimerization rate. A higher current density leads to a faster generation of CO and, as a result, a higher local concentration of CO, which results in a higher dimerization rate and C_2 selectivity. The cell voltage increases with an increase in the current density, as a result of a higher overpotential for both anodic and cathodic reactions, as well as a larger ohmic voltage drop, as shown in Fig. 7d. It is worth noting that the cell voltages are relatively lower compared to those reported in the literature for similar current densities and selectivity [37], indicating that the

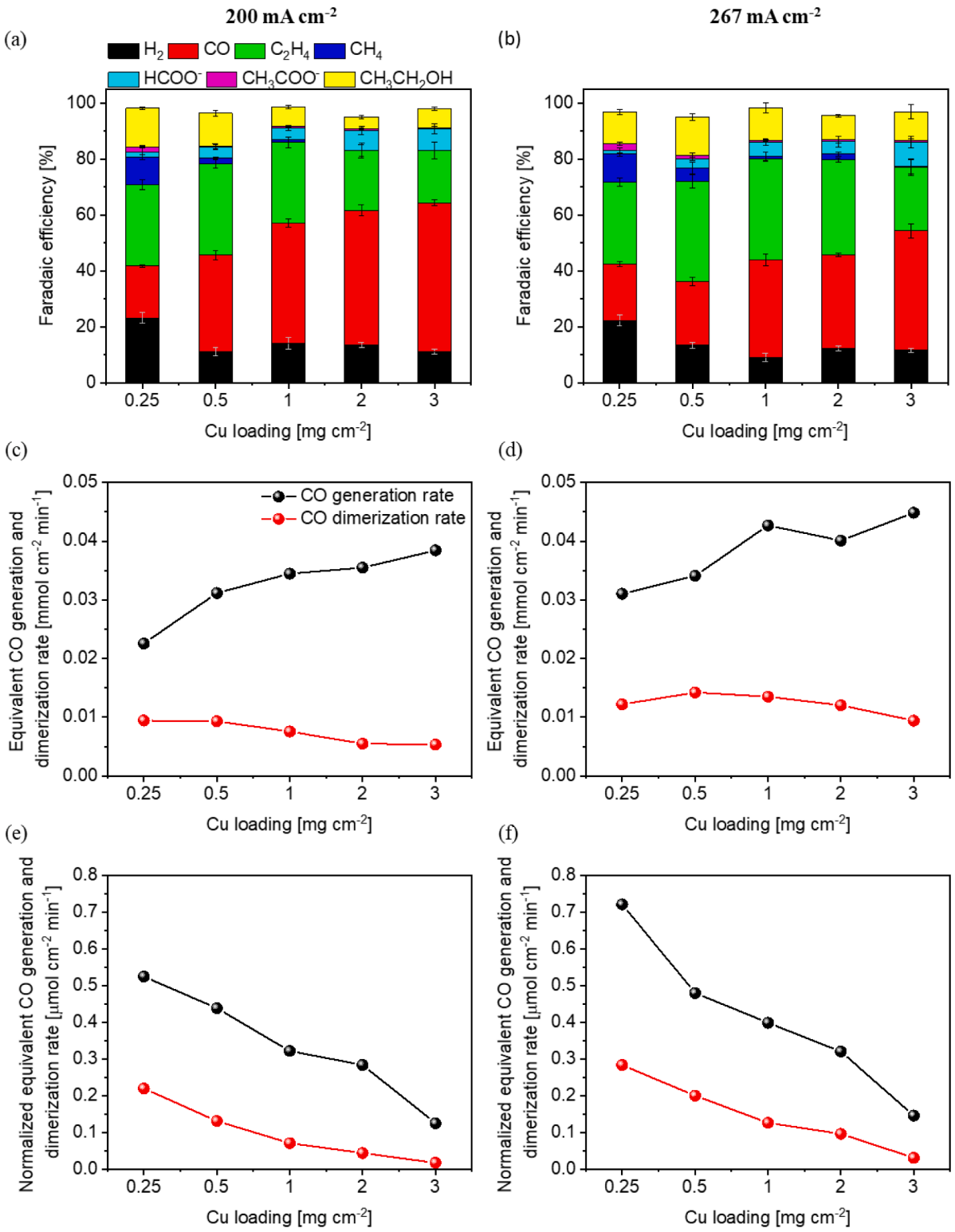

Fig. 6. Comparison of 50 nm NPs electrodes with different loadings: at 200 mA cm^{-2} (a) selectivity, (c) equivalent bulk CO generation and dimerization rates and (e) ECSA-normalized equivalent CO generation and dimerization rates; at 267 mA cm^{-2} (b) selectivity, (d) equivalent bulk CO generation and dimerization rates and (f) ECSA-normalized equivalent CO generation and dimerization rates. Each electrode was tested at least twice. The bulk and ECSA-normalized equivalent CO generation and dimerization rates in (c)-(f) were calculated based on the average values of selectivity of at least two sets of experiments at each catalyst loading and current density.

Cu25_1.0 electrodes can produce C_2 products with a relatively higher energy efficiency (EE). The values of EE are calculated through Eq. (2) and reported in Figure S9. It is noticed that the EE for C_2 products in the two-electrode configuration is around 15–20% at current densities higher than 200 mA cm^{-2}, which is much higher than the 10% reported in simile work at comparable current densities [37] and especially at high current densities > 500 mA cm^{-2} [45].

A stability study has been performed on the Cu25_1.0 electrodes at

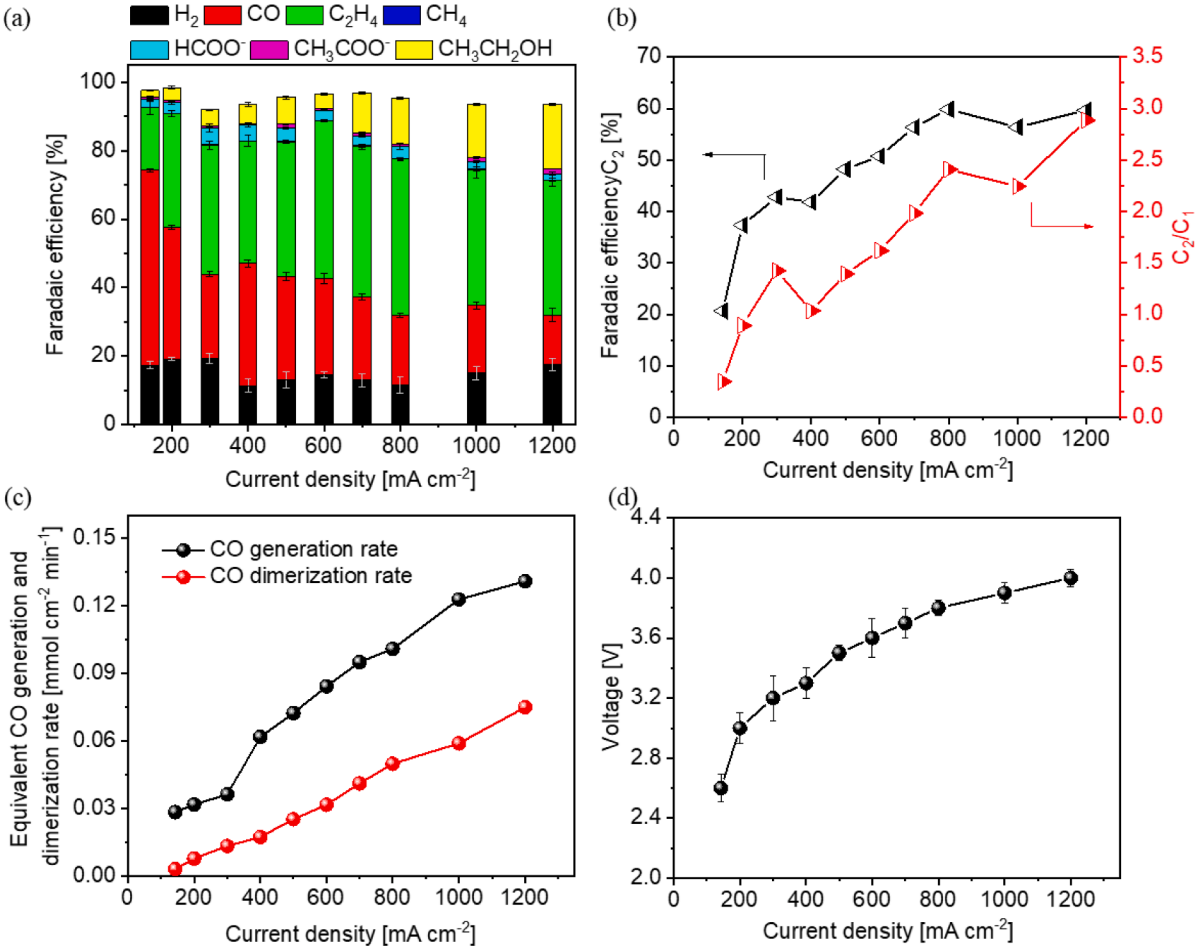

Fig. 7. CO_2RR on Cu25_1.0 electrode at a wide range of current density: (a) product distribution, (b) C_2 selectivity and C_2/C_1 ratio, (c) equivalent CO generation and dimerization rates and (d) cell voltage as a function of the applied current density. Each electrode was tested at least twice. The C_2 selectivity and C_2/C_1 ratio, and equivalent CO generation and dimerization rates in (b) and (c) were calculated based on the average values of selectivity of at least two sets of experiments at each current density.

300 and 600 mA cm^{-2}, respectively. Fig. 8 shows the voltage and product distribution as a function of time at both current densities. The potential is almost constant, while the selectivity is not stable at each current density, and a higher current density leads to a lower stability in the product distribution. The performance is characterized by a changeover in the selectivity from the CO_2RR to the HER, indicating that the stability issue is more related to the flooding of the electrode. In the literature, it is widely reported that the flooding of the GDL electrodes is typically observed in the first several hours of electrolysis, resulting in a significant decline in the selectivity for CO_2RR products [46,47]. When the GDL electrode is flooded, the liquid electrolyte fulfilled a part of the initially hydrophobic pores, not only compromising CO_2 diffusion to active sites on the catalyst surface, but also causing salt precipitation and further choking the pore irreversibly. Recently, the durability has emerged as one of the critical issues to be resolved before further commercialization of CO_2 conversion and it attracts much attention. Leonard et al. [48] reported that the flooding phenomenon could be associated with the total charge passed through the electrodes. A longer electrolysis and a higher current density can cause more severe flooding, due to more OH^-/CO_2 interaction. However, Jouny et al. [49] also observed GDL electrode flooding for CO reduction reaction using KOH as electrolyte where no OH^-/CO_2 interaction exists. In this case, the flooding is considered to be related to the condensation of water vapor. Yang et al. [50] sustained that the applied potential plays a critical role in the flooding advent of GDL electrodes. CO_2RR usually requires high overpotentials, which induce HER on the GDL carbon support and impact the wetting properties of the originally hydrophobic GDL. From this point of view, the operating of CO_2 electrolysis in a low overpotential range, enabled by implementation of high-performance catalytic materials, could improve the stability of CO_2RR.

4. Conclusion

In this work, two families of electrodes fabricated from Cu NPs of different sizes (25 and 50 nm) and characterized by various loadings (between 0.25 and 3.0 mg cm^{-2}) were tested as CO_2RR catalysts. Both classes of electrodes show a variation in selectivity as the loading changes. CH_4 is found to be the main reduction product at very low loadings, while CO is prevalent at higher loadings. For intermediate values (0.5 to 1.0 mg cm^{-2}), the highest selectivity toward C_2H_4 is observed. This behavior can be explained by considering that for very low loadings, the presence of small density NPs, with relatively large distance between active sites, makes the dimerization of CO less likely, favoring instead its hydrogenation toward CH_4 production. By increasing the loading, the higher rate of bulk CO generation makes the dimerization more likely, thus increasing the C_2H_4 production. However, EIS analysis reveals that with further increase in NP loading, the influence of capacitance becomes dominant, thus slowing down the flow of charges from the electrode. This limits the further reduction of CO produced near the active sites, thus making it the main product at higher loadings. Cu25_1.0 electrodes were further tested at different current densities up to 1200 mA cm^{-2} in order to maximize the C_2H_4

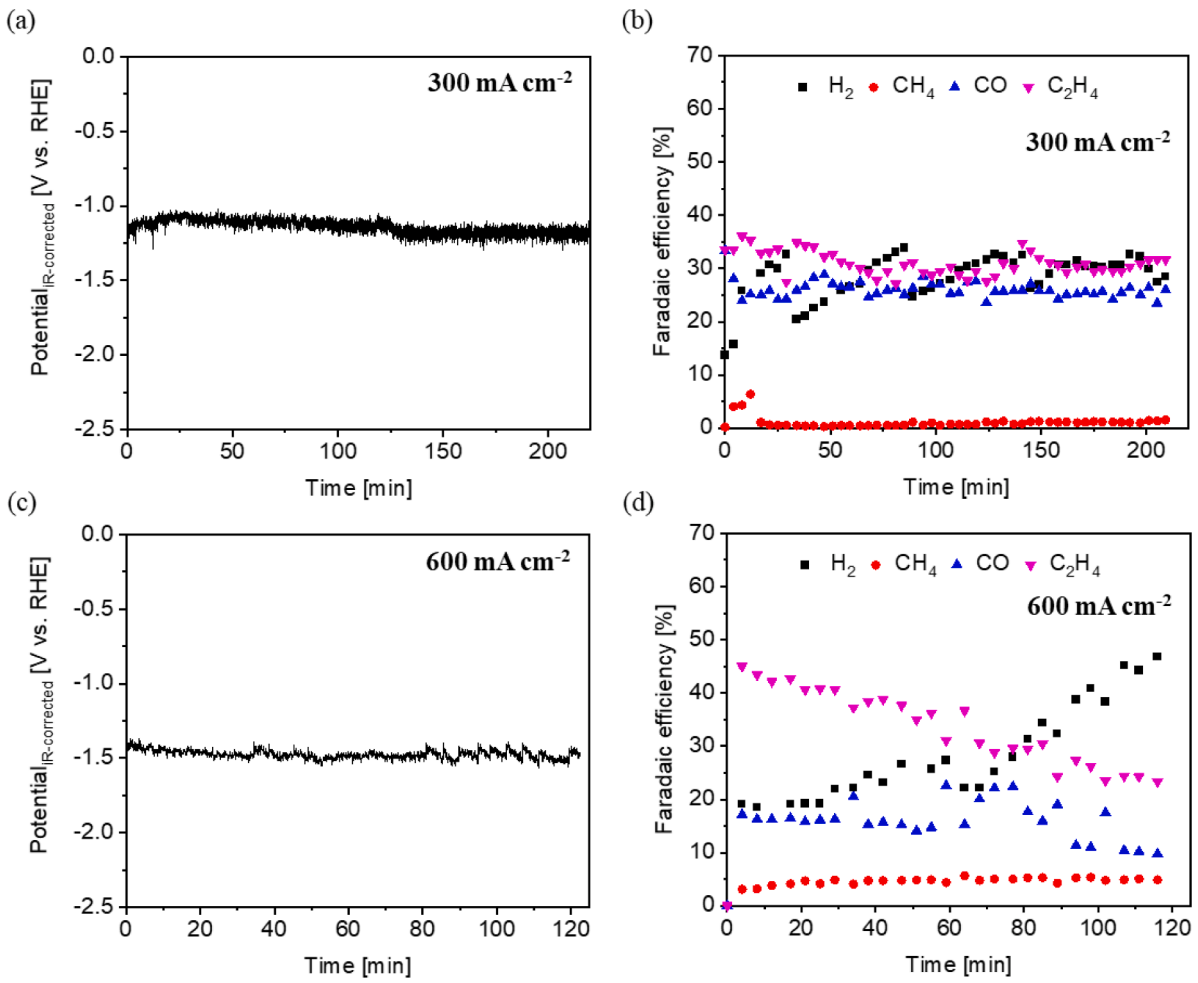

Fig. 8. Long-term CO_2RR on Cu25_1.0 electrodes: 300 mA cm^{-2} (a) voltage as a function of time and (b) product distribution as a function of time; 600 mA cm^{-2} (c) voltage as a function of time and (d) product distribution as a function of time.

production. FE_{C2H4} values higher than 35% are obtained over the studied current density range, with a maximum of 46% at 600 mA cm^{-2}. Both CO generation and dimerization rates raise with increasing current, so that the selectivity toward C_2 products shows the same trend. This result, together with the relatively low cell voltage (< 4.0 V), reveals that the Cu25_1.0 electrodes are capable of producing C_2 molecules with good energy efficiency.

CRediT authorship contribution statement

Juqin Zeng: Conceptualization, Methodology, Validation, Visualization, Supervision, Investigation, Writing – original draft, Writing – review & editing. **Manlio Mignosa:** Investigation, Data curation, Validation, Writing – review & editing. **Nicolò B.D. Monti:** Investigation, Writing – review & editing. **Adriano Sacco:** Visualization, Supervision, Methodology, Writing – review & editing. **Candido F. Pirri:** Resources, Project administration, Visualization, Supervision.

Declaration of Competing Interest

The authors declare that they have no known competing financial interests or personal relationships that could have appeared to influence the work reported in this paper.

Data availability

Data will be made available on request.

Supplementary materials

Supplementary material associated with this article can be found, in the online version, at doi:10.1016/j.electacta.2023.142862.

References

[1] C. Costentin, M. Robert, J.M Savéant, Catalysis of the electrochemical reduction of carbon dioxide, Chem. Soc. Rev. 42 (2013) 2423–2436, https://doi.org/10.1039/C2CS35360A.
[2] A.M. Appel, J.E. Bercaw, A.B. Bocarsly, H. Dobbek, D.L. DuBois, M. Dupuis, et al., Frontiers, opportunities, and challenges in biochemical and chemical catalysis of CO_2 fixation, Chem. Rev. 113 (2013) 6621–6658, https://doi.org/10.1021/cr300463y.
[3] N.B.D. Monti, M. Fontana, A. Sacco, A. Chiodoni, A. Lamberti, C.F. Pirri, et al., Facile fabrication of Ag Electrodes for CO_2-to-CO conversion with near-unity selectivity and high mass activity, ACS Appl. Energy Mater. 5 (2022) 14779–14788, https://doi.org/10.1021/acsaem.2c02143.
[4] M.A.O. Lourenço, J. Zeng, P. Jagdale, M. Castellino, A. Sacco, M.A. Farkhondehfal, et al., Biochar/zinc oxide composites as effective catalysts for electrochemical CO_2 reduction, ACS Sustain. Chem. Eng. 9 (2021) 5445–5453, https://doi.org/10.1021/acssuschemeng.1c00837.
[5] J. Zeng, T. Rino, K. Bejtka, M. Castellino, A. Sacco, M.A. Farkhondehfal, et al., Coupled copper–zinc catalysts for electrochemical reduction of carbon dioxide, ChemSusChem 13 (2020) 4128–4139, https://doi.org/10.1002/cssc.202000971.
[6] K. Bejtka, J. Zeng, A. Sacco, M. Castellino, S. Hernández, M.A. Farkhondehfal, et al., Chainlike mesoporous SnO_2 as a well-performing catalyst for electrochemical CO_2 reduction, ACS Appl. Energy Mater. 2 (2019) 3081–3091, https://doi.org/10.1021/acsaem.8b02048.
[7] J. Zeng, P. Jagdale, M.A.O. Lourenço, M.A. Farkhondehfal, D. Sassone, M. Bartoli, et al., Biochar-supported BiO_x for effective electrosynthesis of formic acid from carbon dioxide reduction, Crystals 11 (2021) 363, https://doi.org/10.3390/cryst11040363.

[8] S. Zhao, R. Jin, R. Jin, Opportunities and challenges in CO_2 reduction by gold- and silver-based electrocatalysts: from bulk metals to nanoparticles and atomically precise nanoclusters, ACS Energy Lett 3 (2018) 452–462, https://doi.org/10.1021/acsenergylett.7b01104.

[9] A. Bagger, W. Ju, A.S. Varela, P. Strasser, J. Rossmeisl, Electrochemical CO_2 reduction: a classification problem, ChemPhysChem 18 (2017) 3266–3273, https://doi.org/10.1002/cphc.201700736.

[10] R.I. Masel, Z. Liu, H. Yang, J.J. Kaczur, D. Carrillo, S. Ren, et al., An industrial perspective on catalysts for low-temperature CO_2 electrolysis, Nat. Nanotechnol. 16 (2021) 118–128, https://doi.org/10.1038/s41565-020-00823-x.

[11] D. Johnson, Z. Qiao, A. Djire, Progress and challenges of carbon dioxide reduction reaction on transition metal based electrocatalysts, ACS Appl. Energy Mater. 4 (2021) 8661–8684, https://doi.org/10.1021/acsaem.1c01624.

[12] X. Wang, A. Xu, F. Li, S.F. Hung, D.H Nam, C.M. Gabardo, et al., Efficient methane electrosynthesis enabled by tuning local CO_2 availability, J. Am. Chem. Soc. 142 (2020) 3525–3531, https://doi.org/10.1021/jacs.9b12445.

[13] Z. Chen, P. Li, R. Anderson, X. Wang, X. Zhang, L. Robison, et al., Balancing volumetric and gravimetric uptake in highly porous materials for clean energy, Science 368 (2020) 297–303, https://doi.org/10.1126/science.aaz8881.

[14] J. Sisler, S. Khan, A.H. Ip, M.W. Schreiber, S.A. Jaffer, E.R. Bobicki, et al., Ethylene electrosynthesis: a comparative techno-economic analysis of alkaline vs membrane electrode assembly vs CO_2–CO–C_2H_4 tandems, ACS Energy Lett. 6 (2021) 997–1002, https://doi.org/10.1021/acsenergylett.0c02633.

[15] R. Reske, H. Mistry, F. Behafarid, B. Roldan Cuenya, P Strasser, Particle size effects in the catalytic electroreduction of CO_2 on Cu nanoparticles, J. Am. Chem. Soc. 136 (2014) 6978–6986, https://doi.org/10.1021/ja500328k.

[16] T.T.H. Hoang, S. Verma, S. Ma, T.T. Fister, J. Timoshenko, A.I. Frenkel, et al., Nanoporous copper–silver alloys by additive-controlled electrodeposition for the selective electroreduction of CO_2 to ethylene and ethanol, J. Am. Chem. Soc. 140 (2018) 5791–5797, https://doi.org/10.1021/jacs.8b01868.

[17] K.D. Yang, W.R. Ko, J.H. Lee, S.J. Kim, H. Lee, M.H. Lee, et al., Morphology-directed selective production of ethylene or ethane from CO_2 on a Cu mesopore electrode, Angew. Chem. Int. Edit. 56 (2017) 796–800, https://doi.org/10.1002/anie.201610432.

[18] P. Iyengar, J. Huang, G.L. De Gregorio, C. Gadiyar, R. Buonsanti, Size dependent selectivity of Cu nano-octahedra catalysts for the electrochemical reduction of CO_2 to CH_4, Chem. Commun. 55 (2019) 8796–8799, https://doi.org/10.1039/C9CC02522G.

[19] H. Bai, T. Cheng, S. Li, Z. Zhou, H. Yang, J. Li, et al., Controllable CO adsorption determines ethylene and methane productions from CO_2 electroreduction, Sci. Bull. 66 (2021) 62–68, https://doi.org/10.1016/j.scib.2020.06.023.

[20] T.C. Chou, C.C. Chang, H.L. Yu, W.Y. Yu, C.L. Dong, J.J. Velasco-Vélez, et al., Controlling the oxidation state of the Cu electrode and reaction intermediates for electrochemical CO_2 reduction to ethylene, J. Am. Chem. Soc. 142 (2020) 2857–2867, https://doi.org/10.1021/jacs.9b11126.

[21] J. Zhang, Z. Li, R. Cai, T. Zhang, S. Yang, L. Ma, et al., Switching CO_2 electroreduction selectivity between C_1 and C_2 hydrocarbons on Cu gas-diffusion electrodes, Energy Environ. Mater. 2 (2023) e12307, https://doi.org/10.1002/eem2.12307.

[22] M. Favaro, H. Xiao, T. Cheng, W.A. Goddard, J. Yano, E.J. Crumlin, Subsurface oxide plays a critical role in CO_2 activation by Cu(111) surfaces to form chemisorbed CO_2, the first step in reduction of CO_2, Proc. Natl. Acad. Sci. 114 (2017) 6706–6711, https://doi.org/10.1073/pnas.1701405114.

[23] C. Tang, J. Shi, X. Bai, A. Hu, N. Xuan, Y. Yue, et al., CO_2 reduction on copper's twin boundary, ACS Catal 10 (2020) 2026–2032, https://doi.org/10.1021/acscatal.9b03814.

[24] Y. Xu, F. Li, A. Xu, J.P. Edwards, S.F. Hung, C.M. Gabardo, et al., Low coordination number copper catalysts for electrochemical CO_2 methanation in a membrane electrode assembly, Nat. Commun. 12 (2021) 2932, https://doi.org/10.1038/s41467-021-23065-4.

[25] D.A. Henckel, M.J. Counihan, H.E. Holmes, X. Chen, U.O. Nwabara, S. Verma, et al., Potential dependence of the local pH in a CO_2 reduction electrolyzer, ACS Catal. 11 (2021) 255–263, https://doi.org/10.1021/acscatal.0c04297.

[26] T. Zhang, Z. Li, J. Zhang, J. Wu, Enhance CO_2-to-C_{2+} products yield through spatial management of CO transport in Cu/ZnO tandem electrodes, J. Catal. 387 (2020) 163–169, https://doi.org/10.1016/j.jcat.2020.05.002.

[27] S. Zhang, S. Zhao, D. Qu, X. Liu, Y. Wu, Y. Chen, et al., Electrochemical Reduction of CO_2 Toward C_2 Valuables on Cu@Ag Core-Shell Tandem Catalyst with Tunable Shell Thickness, Small 17 (2021), 2102293, https://doi.org/10.1002/smll.202102293.

[28] N.T. Suen, Z.R. Kong, C.S. Hsu, H.C. Chen, C.W. Tung, Y.R. Lu, et al., Morphology manipulation of copper nanocrystals and product selectivity in the electrocatalytic reduction of carbon dioxide, ACS Catal. 9 (2019) 5217–5222, https://doi.org/10.1021/acscatal.9b00790.

[29] B. Zhang, J. Zhang, P. An, Z. Su, Q. Wan, X. Tan, et al., Steering CO_2 electroreduction toward methane or ethylene production, Nano Energy 88 (2021), 106239, https://doi.org/10.1016/j.nanoen.2021.106239.

[30] J. Zeng, J.R. Nair, C. Francia, S. Bodoardo, N. Penazzi, Aprotic Li–O_2 cells: gas diffusion layer (GDL) as catalyst free cathode and tetraglyme/$LiClO_4$ as electrolyte, Solid State Ion 262 (2014) 160–164, https://doi.org/10.1016/j.ssi.2013.09.032.

[31] S. Martinez Crespiera, D. Amantia, E. Knipping, C. Aucher, L. Aubouy, J. Amici, et al., Electrospun Pd-doped mesoporous carbon nano fibres as catalysts for rechargeable Li–O_2 batteries, RSC Adv 6 (2016) 57335–57345, https://doi.org/10.1039/C6RA09721A.

[32] J. Zeng, M.R. Fiorentin, M. Fontana, M. Castellino, F. Risplendi, A. Sacco, et al., Novel insights into Sb-Cu Catalysts for electrochemical reduction of CO_2, Appl. Catal. B Environ. 306 (2022), 121089, https://doi.org/10.1016/j.apcatb.2022.121089.

[33] S. Nitopi, E. Bertheussen, S.B. Scott, X. Liu, A.K. Engstfeld, S. Horch, et al., Progress and perspectives of electrochemical CO_2 reduction on copper in aqueous electrolyte, Chem. Rev. 119 (2019) 7610–7672, https://doi.org/10.1021/acs.chemrev.8b00705.

[34] J. Zeng, K. Bejtka, W. Ju, M. Castellino, A. Chiodoni, A. Sacco, et al., Advanced Cu-Sn foam for selectively converting CO_2 to CO in aqueous solution, Appl. Catal. B Environ. 236 (2018) 475–482, https://doi.org/10.1016/j.apcatb.2018.05.056.

[35] J. Zeng, M. Castellino, K. Bejtka, A. Sacco, G. Di Martino, M.A. Farkhondehfal, et al., Facile synthesis of cubic cuprous oxide for electrochemical reduction of carbon dioxide, J. Mater. Sci. 56 (2021) 1255–1271, https://doi.org/10.1007/s10853-020-05278-y.

[36] P. Waszczuk, P. Zelenay, J. Sobkowski, Surface interaction of benzoic acid with a copper electrode, Electrochim. Acta 40 (1995) 1717–1721, https://doi.org/10.1016/0013-4686(95)00088-V.

[37] E. Jeng, Z. Qi, A.R. Kashi, S. Hunegnaw, Z. Huo, J.S. Miller, et al., Scalable gas diffusion electrode fabrication for electrochemical CO_2 reduction using physical vapor deposition methods, ACS Appl. Mater. Interfaces 14 (2022) 7731–7740, https://doi.org/10.1021/acsami.1c17860.

[38] S. Trasatti, O.A. Petrii, Real surface area measurements in electrochemistry, Pure Appl. Chem. 63 (1991) 711–734, https://doi.org/10.1351/pac199163050711.

[39] W. Ju, J. Zeng, K. Bejtka, H. Ma, D. Rentsch, M. Castellino, et al., Sn-decorated Cu for selective electrochemical CO_2 to CO conversion: precision architecture beyond composition design, ACS Appl. Energy Mater. 2 (2019) 867–872, https://doi.org/10.1021/acsaem.8b01944.

[40] A. Sacco, Electrochemical impedance spectroscopy as a tool to investigate the electroreduction of carbon dioxide: a short review, J. CO_2 Util. 27 (2018) 22–31, https://doi.org/10.1016/j.jcou.2018.06.020.

[41] U. Savino, A. Sacco, K. Bejtka, M. Castellino, M.A. Farkhondehfal, A. Chiodoni, et al., Well performing Fe-SnO_2 for CO_2 reduction to HCOOH, Catal. Commun. 163 (2022), 106412, https://doi.org/10.1016/j.catcom.2022.106412.

[42] Y. Zhong, X. Kong, Z. Song, Y. Liu, L. Peng, L. Zhang, et al., Adjusting Local CO Confinement in porous-shell Ag@Cu catalysts for enhancing C–C coupling toward CO_2 eletroreduction, Nano Lett. 22 (2022) 2554–2560, https://doi.org/10.1021/acs.nanolett.1c04815.

[43] T. Zhang, J.C. Bui, Z. Li, A.T. Bell, A.Z. Weber, J. Wu, Highly selective and productive reduction of carbon dioxide to multicarbon products via in situ CO management using segmented tandem electrodes, Nat. Catal. 5 (2022) 202–211, https://doi.org/10.1038/s41929-022-00751-0.

[44] X. Zhou, J. Shan, L. Chen, B.Y. Xia, T. Ling, J. Duan, et al., Stabilizing Cu_{2+} ions by solid solutions to promote CO_2 electroreduction to methane, J. Am. Chem. Soc. 144 (2022) 2079–2084, https://doi.org/10.1021/jacs.1c12212.

[45] X. She, T. Zhang, Z. Li, H. Li, H. Xu, J. Wu, Tandem electrodes for carbon dioxide reduction into C_{2+} products at simultaneously high production efficiency and rate, Cell Rep. Phys. Sci. 1 (2020), 100051, https://doi.org/10.1016/j.xcrp.2020.100051.

[46] P. Jeanty, C. Scherer, E. Magori, K. Wiesner-Fleischer, O. Hinrichsen, M. Fleischer, Upscaling and continuous operation of electrochemical CO_2 to CO conversion in aqueous solutions on silver gas diffusion electrodes, J. CO_2 Util. 24 (2018) 454–462, https://doi.org/10.1016/j.jcou.2018.01.011.

[47] B. De Mot, J. Hereijgers, M. Duarte, T. Breugelmans, Influence of flow and pressure distribution inside a gas diffusion electrode on the performance of a flow-by CO_2 electrolyzer, Chem. Eng. J. 378 (2019), 122224, https://doi.org/10.1016/j.cej.2019.122224.

[48] M.E. Leonard, L.E. Clarke, A. Forner-Cuenca, S.M. Brown, F.R. Brushett, Investigating electrode flooding in a flowing electrolyte, gas-fed carbon dioxide electrolyzer, ChemSusChem 13 (2020) 400–411, https://doi.org/10.1002/cssc.201902547.

[49] M. Jouny, W. Luc, F. Jiao, High-rate electroreduction of carbon monoxide to multi-carbon products, Nat. Catal. 1 (2018) 748–755, https://doi.org/10.1038/s41929-018-0133-2.

[50] K. Yang, R. Kas, W.A. Smith, T. Burdyny, Role of the carbon-based gas diffusion layer on flooding in a gas diffusion electrode cell for electrochemical CO_2 reduction, ACS Energy Lett. 6 (2021) 33–40, https://doi.org/10.1021/acsenergylett.0c02184.